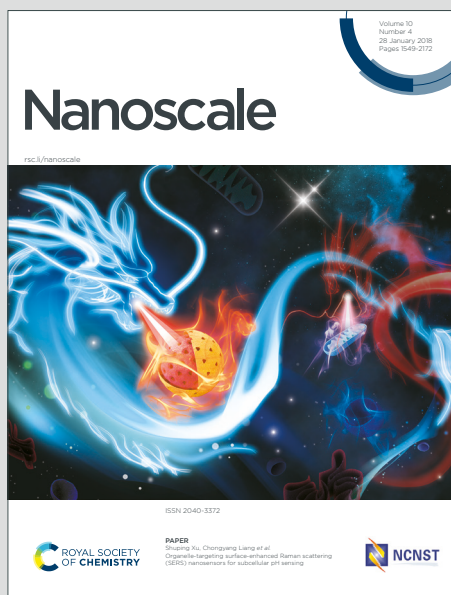


Nanoscale

Accepted Manuscript

This article can be cited before page numbers have been issued, to do this please use: J. Zhou, S. Zhang, H. Dong, Y. Li, H. Zang, Z. Teng, M. Zhang, Y. Liu, S. Sun and H. Guo, *Nanoscale*, 2026, DOI: 10.1039/D5NR04283F.



This is an Accepted Manuscript, which has been through the Royal Society of Chemistry peer review process and has been accepted for publication.

Accepted Manuscripts are published online shortly after acceptance, before technical editing, formatting and proof reading. Using this free service, authors can make their results available to the community, in citable form, before we publish the edited article. We will replace this Accepted Manuscript with the edited and formatted Advance Article as soon as it is available.

You can find more information about Accepted Manuscripts in the [Information for Authors](#).

Please note that technical editing may introduce minor changes to the text and/or graphics, which may alter content. The journal's standard [Terms & Conditions](#) and the [Ethical guidelines](#) still apply. In no event shall the Royal Society of Chemistry be held responsible for any errors or omissions in this Accepted Manuscript or any consequences arising from the use of any information it contains.

ARTICLE

Received 00th January 20xx,
Accepted 00th January 20xx

DOI: 10.1039/x0xx00000x

Mn²⁺-Coordinated Glycyrrhizic Acid Self-Adjuvating Hydrogel for Sustained Codelivery of Antigen and Mn²⁺ for a Potent Immune ResponseJingjing Zhou^a, Shengying Zhang^a, Hu Dong^a, Yunhua Li^b, Haoyue Zang^a, Zhidong Teng^a, Mingyang Zhang^a, Yifan Liu^a, Shiqi Sun^{a*}, Huichen Guo^{a*}

The development of vaccine platforms that enable sustained codelivery of antigens and adjuvants remains a major challenge in modern vaccinology. Herein, we constructed a self-adjuvating hydrogel (GA@Mn) via the self-assembly of natural glycyrrhizic acid (GA) and subsequent coordination with Mn²⁺. This coordination facilitates gradual Mn²⁺ release during hydrogel degradation, overcoming the rapid clearance and poor bioavailability of soluble Mn²⁺ *in vivo*. Notably, Mn²⁺ coordination drastically increased the crosslinking density of GA hydrogel (GAgel) network, enhancing storage modulus of GA@Mn by three orders of magnitude compared to the native GAgel. This superior mechanical stability allows GA@Mn to serve as an efficient antigen depot, prolonging the retention of both Mn²⁺ and antigen at the injection site for up to 14 days. Meanwhile, GA@Mn promoted robust local immune cell recruitment, establishing an antigen-presenting cell (APC)-rich microenvironment. Subsequently, GA@Mn activation of the STING pathway enhanced dendritic cell (DC) maturation and antigen uptake by 2.4-fold and 1.8-fold, respectively. In mice, a single injection of GA@Mn significantly potentiated antigen-specific humoral and cellular immune responses, leveraging a synergistic effect between the STING-activating capacity of Mn²⁺ and the depot-forming ability of the hydrogel.

In summary, this study presents a facilely fabricated GA@Mn hydrogel vaccine platform that enables sustained codelivery of antigen and adjuvant (Mn²⁺) for robust immune enhancement. This work provides a new paradigm for the rational design of metal ion-coordinated hydrogel vaccine.

1. Introduction

Viruses cause a broad range of infectious

diseases, which include conditions ranging from seasonal influenza to COVID-19, and often lead to considerable medical, economic, and social

^a State Key Laboratory of Animal Disease Control and Prevention, College of Veterinary Medicine, Lanzhou University, Lanzhou Veterinary Research Institute, Chinese Academy of Agricultural Sciences, Lanzhou, China.

^b College of Chemistry and Chemical Engineering, Lanzhou University, Lanzhou, China.

*Corresponding authors: sunshiqi@caas.cn (S. Sun); guohuichen@caas.cn (H. Guo);

ARTICLE

Journal Name

consequences. Vaccination remains the most effective strategy for preventing viral infections.¹ The protective efficacy of vaccines depends on adaptive immunity, which is synergistically initiated by antigens and adjuvants. By facilitating antigen depot formation, enabling targeted delivery, activating immune cells, and promoting antigen uptake, adjuvants play an essential role in modulating immune response profiles. These functions collectively contribute to enhanced vaccine potency, reduced antigen dosage, and lower production costs.^{2,3} Despite their importance, adjuvant development has advanced slowly since the introduction of aluminum-based adjuvants (alum) in the 1920s, and it continues to lag far behind progress in antigen design. To date, only a limited number of adjuvants have been approved for clinical use.⁴ Therefore, there is an urgent need for novel adjuvants that exhibit simple composition and clearly defined mechanisms.

Manganese (Mn^{2+}), which is an essential trace element, plays vital roles in development, metabolism, and the maintenance of antioxidant homeostasis.⁵ Notably, Jiang et al. revealed that Mn^{2+} potently activates the endoplasmic reticulum STING pathway, thereby triggering downstream signaling that stimulates the production of type I interferons (IFNs) and pro-inflammatory cytokines while also promoting the maturation of dendritic cells (DCs) and macrophages for enhanced antigen presentation.^{6,7} These properties establish Mn^{2+} as a highly promising adjuvant candidate, particularly in its capacity to bolster Th1-mediated cellular immunity. However, free Mn^{2+} injected *in vivo* rapidly diffuses from the injection site into systemic circulation, where it is subject to swift metabolism and excretion, significantly limiting its immunostimulatory potential.⁸ It is therefore critical to incorporate Mn^{2+} into a delivery system that ensures sustained release in order to maximize its adjuvant efficacy, which represents a major hurdle for the clinical translation of metal ion-based adjuvants.

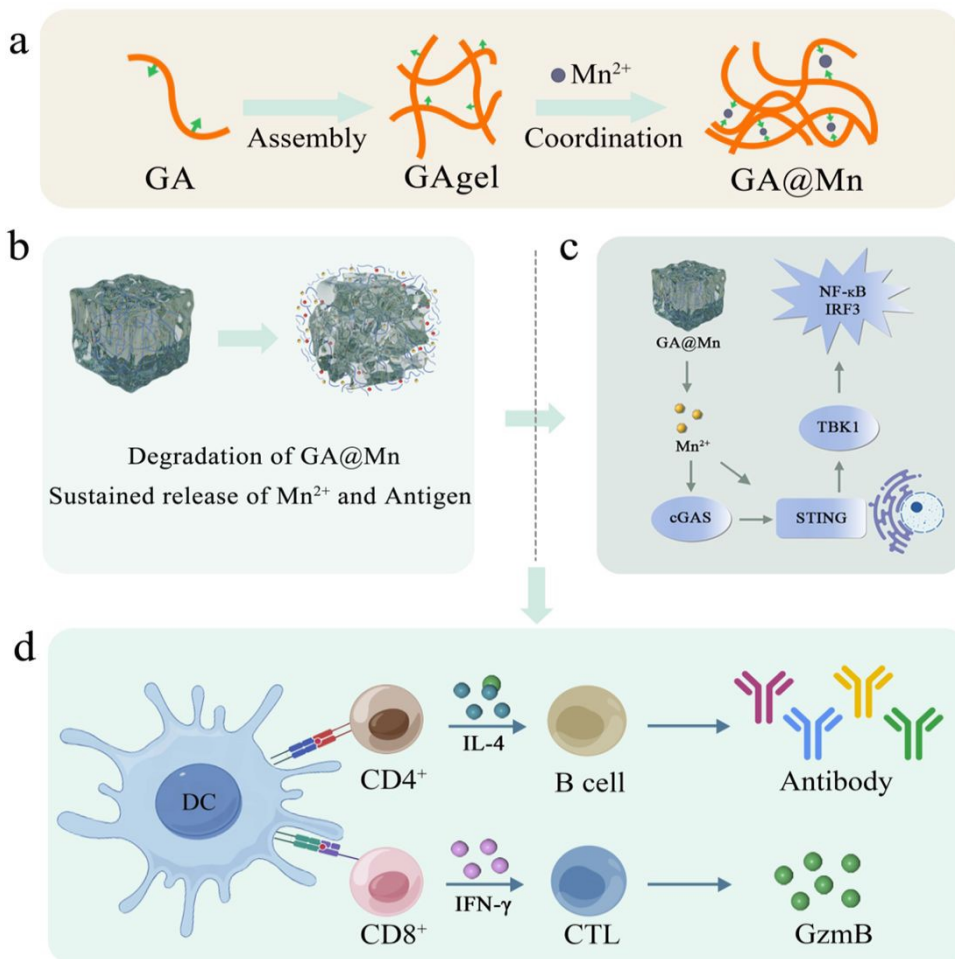
Self-assembly of free drugs into nanomedicines represents a promising strategy for achieving controlled delivery.⁹ While various materials, such as nanoparticles, electrospun fibers, emulsions, and

hydrogels, have been employed for antigen and adjuvant delivery,^{10,11} many conventional systems often lack the structural features needed for efficient signaling interactions with surrounding cells or tissues.¹² Hydrogels possess a porous, nanofibrous architecture that mimics the extracellular matrix, serving as scaffolds that support cell migration, immune cell recruitment, and localized antigen processing and presentation.¹³⁻¹⁵ Their solid-like nature allows the formation of persistent depots at the injection site, which may enhance Th2-biased humoral immunity.¹⁶ Among them, hydrogels formed through direct self-assembly of natural small molecules have attracted interest due to their simple preparation and favorable biocompatibility.^{17,18} These carrier-free systems eliminate the need for exogenous crosslinkers and allow gentle antigen incorporation via mixing, holding significant potential for vaccine applications.¹⁹ Glycyrrhizic acid (GA), a natural amphiphile derived from traditional Chinese medicine, consists of a hydrophobic triterpenoid aglycone (18β -glycyrrhetic acid) and a hydrophilic diglucuronic acid unit, enabling its self-assembly in aqueous solution into low-molecular-weight hydrogels.²⁰⁻²² However, almost all hydrogel platforms are unable to achieve the sustained co-delivery of antigens and adjuvants, which is crucial for inducing a potent immune response. Metal ion coordination provides a robust alternative for engineering hydrogel systems, where the coordinated ions not only facilitate molecular assembly but also serve as inherent immune adjuvants.^{23,24} Inspired by this approach, we developed a coordination-mediated coassembly strategy between GA and Mn^{2+} . As illustrated in Scheme 1, Mn^{2+} coordination facilitated the formation of a reinforced hydrogel designated GA@Mn. Then, we systematically investigated its formation mechanism, rheological properties, and sustained release profile for both antigen and Mn^{2+} . In our previous work, we successfully prepared Foot-and-Mouth Disease Virus-Like Particles (FMD VLPs) with an average diameter of 25 nm using an *E. coli* expression system. These VLPs elicited robust protective immune responses in guinea pigs, pigs, and cattle.²⁵ Here, we loaded FMD VLPs into the GA@Mn hydrogel and

comprehensively evaluated its ability to activate innate immunity, recruit and mature immune cells, and elicit antigen-specific humoral and cellular

serum (FBS) were obtained from Gibco (USA). ³ (4,5-Dimethylthiazol-2-yl)-5-(3-carboxymethoxyphenyl)-2-(4-sulfophenyl)-2H-

DOI: 10.1039/D5NR04283F



Scheme 1. Schematic of GA@Mn hydrogel preparation and biological function. **(a)** Mn²⁺ coordination-driven GA@Mn hydrogel formation. **(b)** Gradual degradation of GA@Mn with sustained Mn²⁺ and antigen release. **(c)** The STING pathway was activated by released Mn²⁺. **(d)** GA@Mn vaccine platform eliciting robust humoral and cellular immunity.

immune responses.

2. Experimental

2.1. Materials

Manganese chloride tetrahydrate (MnCl₂·4H₂O) was purchased from Shanghai Macklin Biochemical Co., Ltd. (China). GA (C₄₂H₆₂O₁₆) was purchased from Beijing Solarbio Science & Technology Co., Ltd. (China). Dulbecco's Modified Eagle Medium (DMEM) and fetal bovine

tetrazolium, inner salt (MTS) was purchased from Promega (China). The Calcein-AM/PI double stain kit was purchased from Solarbio (China). The pre-coated mouse IFN-γ ELISpot kit was purchased from Dakewei (China), and the mouse GzmB ELISA kit was purchased from mlbio (China). Mouse OVA-IgG, OVA-IgG1, and OVA-IgG2a ELISA Kits were purchased from mlbio (Shanghai, China).

2.2. Animals

ARTICLE

Journal Name

Female BALB/c mice (6-8 weeks old, weighing 18-22 g) were obtained from the Laboratory Animal Center of the Lanzhou Veterinary Research Institute, Chinese Academy of Agricultural Sciences. Mice were housed under standard temperature-controlled conditions with ad libitum access to food and water. The minimum number of animals necessary was used, and all efforts were made to minimize distress. Following experimental procedures, animals were euthanized. All the experiments in this study were carried out under the European Communities Council Directive of 24 November 1986 (86/609/EEC) and were approved by the Animal Management and Ethics Committee of the Lanzhou Veterinary Research Institute, Chinese Academy of Agricultural Sciences (Approval No. LVRIAEC-2024-027).

2.3. Hydrogel Formation

Aqueous solutions of MnCl_2 or AlCl_3 at different concentrations (0, 0.5 mM, 1 mM, 2.5 mM, 5 mM) were added to the GA solution, respectively. The mixtures were cooled to room temperature to obtain GA@Mn or GA@Al hydrogels. The final concentration of GA was 3% (w/v).

2.4. Scanning Electron Microscopy (SEM)

The hydrogel microstructure and Mn^{2+} distribution were characterized using an Apreo S SEM (Thermo Fisher Scientific, USA). Samples were deposited onto silicon wafers and air-dried at room temperature, then sputter-coated with a thin gold layer. SEM imaging and energy-dispersive X-ray spectroscopy (EDS) mapping were performed.

2.5. Isothermal Titration Calorimetry (ITC)

Mn^{2+} binding to GA were measured using a MicroCal PEAQ-ITC instrument (Malvern Instruments, UK). A total of 40 μL of MnCl_2 solution (5 mM) was titrated into 280 μL of GA solution (250 μM) at 25 °C with stirring at 1500 rpm. The protocol consisted of 13 automated injections: an initial 0.4 μL injection followed by 12 injections of 3 μL each, at 150 s intervals. Heat flow was recorded over time, and thermodynamic parameters including dissociation constant (KD), binding stoichiometry (n), and enthalpy change

(ΔH) were calculated using the instrument's software.

2.6. Fourier Transform Infrared (FTIR) Analysis

FTIR spectroscopy was performed on the GA@Mn hydrogels using an FTIR spectrometer (TENSOR 27, Bruker, Germany). Their freeze-dried powders were separately mixed with potassium bromide (KBr) and pressed into pellets. The infrared spectra were then recorded in the wavenumber range of 500 - 4000 cm^{-1} .

2.7. Rheological Analysis

Rheological properties were determined using a HAAKE RS6000 rheometer (Thermo Fisher Scientific, USA) with a 35 mm parallel plate geometry at 25 °C. Tests included: (1) Strain sweep (0.1-100% strain) to define the linear viscoelastic region (LVR). (2) Frequency sweep (0.1-100 rad s^{-1}) at 1% strain. (3) Time sweep at 1% strain and 1 Hz for 900 s. (4) Step-strain injectability tests, three cycles of 5 min at 1% strain followed by 1 min at 100% strain, recording storage modulus (G') and loss modulus (G'').

2.8. Storage Stability of GA@Mn Hydrogel

200 μL of the prepared GA@Mn hydrogel was placed in a 15 mL centrifuge tube. The samples were stored at room temperature for 5 days, 10 days, and 10 months, respectively. Then, photographs were taken to record the hydrogel integrity. SEM and EDS imaging were performed as described in Section 2.4. Finally, time sweep and step-strain tests were carried out as described in Section 2.6 to evaluate the mechanical properties of the hydrogels.

2.9. MTS Cytotoxicity Assay

The cytotoxicity of FMD VLPs, GA@Mn hydrogels was assessed using Vero, DC2.4, and BHK cell lines. Hydrogel leachates were prepared by incubating hydrogels in 1 mL DMEM at 37 °C for 24 h. Cells were seeded 1×10^6 cells per well in 96-well plates and incubated for 24 h before replacing the medium with leachates or control DMEM. After an additional 24 h, 10 μL of



MTS reagent was added and incubated for 2 h. Absorbance at 490 nm was measured (Synergy multi-mode microplate reader, BioTek, USA), and cell viability (%) was calculated as: Cell viability (%) = [OD_{sample}/OD_{control}] × 100.

2.10. Calcein-AM/PI Cytotoxicity Assay

Cells were co-cultured with hydrogel leachates in 24-well plates for 24 h, then stained using the Calcein-AM/PI kit per the manufacturer's instructions. Morphology and density were observed with a TH4-200 fluorescence microscope (Olympus, Japan).

2.11. *In Vitro* Degradation of Hydrogels

The *in vitro* degradation profiles of GAgel and GA@Mn hydrogels were investigated gravimetrically. Hydrogels loaded with FITC-OVA were immersed in 400 μL PBS (0.01 M, pH 7.4), overlaid with an additional 400 μL PBS, and incubated under simulated physiological conditions (37 °C, 60% relative humidity). At 24 h intervals, the supernatant PBS was collected, the residual hydrogel mass was recorded, and fresh PBS of equal volume was added. This cycle was repeated until complete degradation. Degradation behavior was quantified by calculating hydrogel mass retention over time.

2.12. *In Vitro* Antigen Release

The release kinetics of FITC-OVA from GAgel and GA@Mn hydrogels were monitored using fluorescence spectroscopy. Supernatant samples were analyzed at an excitation wavelength of 490 nm and an emission wavelength of 525 nm using an FLS 1000 spectrofluorometer (Edinburgh Instruments, UK). Cumulative antigen release was calculated from fluorescence measurements to generate release profiles.

2.13. *In Vitro* Mn²⁺ Release

Mn²⁺ release from GA@Mn was quantified by inductively coupled plasma mass spectrometry (ICP-MS). Mn²⁺ concentrations in the collected supernatants were measured to determine temporal release profiles.

2.14. *In Vivo* Antigen and Mn²⁺ Biodistribution

BALB/c mice were subcutaneously injected 200 μL of with MnCl₂ containing Cy5-OVA, GAgel loaded with Cy5-OVA, or GA@Mn loaded with Cy5-OVA. At predetermined time points (1, 3, 7, 10, 14, and 21 days post-injection), mice were anesthetized with isoflurane and imaged using an AniView 100 *in vivo* imaging system (Biolight Biotechnology Co., Ltd., China). Antigen biodistribution was evaluated from Cy5 fluorescence signals. Tissues from the injection site and major organs (heart, liver, lung, spleen, kidney) were collected at each time point, and Mn²⁺ content was quantified by ICP-MS. At 0, 0.5, 1, 3, 5, and 10 days post-injection, peripheral blood was collected from the injected mice, and the Mn²⁺ content in the blood was determined by ICP-MS. On days 5 and 10 post-injection, peripheral blood was collected separately from the injected mice for blood biochemical tests. The tested indicators included albumin (ALB), alanine aminotransferase (ALT), aspartate aminotransferase (AST), creatinine (CREA), uric acid (UA), and urea nitrogen (UREA).

2.15. The Expression of STING Pathway-Related Proteins

Western blotting (WB) was employed to analyze the expression levels of proteins associated with the STING signaling pathway. DC2.4 cells were seeded 5 × 10⁵ cells per well in 6-well plates and treated with GAgel leachate, MnCl₂ solution, or GA@Mn leachate; blank medium served as the control. After 12 h, cells were lysed in 1 × SDS denaturing buffer and heat-denatured. Proteins were separated by SDS-PAGE and transferred to PVDF membranes by wet transfer. Membranes were blocked and probed with primary antibodies against phosphor-STING (p-STING), phospho-IRF3 (p-IRF3), phospho-TBK1 (p-TBK1), and β-tubulin. After overnight incubation at 4 °C, membranes were treated with HRP-conjugated goat anti-rabbit secondary antibody for 1 h at room temperature. Bands were visualized by ECL chemiluminescence (Tanon, Shanghai).

2.16. The mRNA Expression of cGAS-STING Pathway Related Cytokines

ARTICLE

Journal Name

Mice were subcutaneously injected with 200 μ L of PBS, FMD VLPs, MnCl₂, GAgel, or GA@Mn, respectively. At 24 h post-injection, injection site tissue was collected, homogenized in Trizol, and processed for RNA extraction. cDNA synthesis and RT-PCR were performed according to the classical methods. GAPDH served as the reference, and relative expression of cGAS-STING pathway related cytokines was calculated using the $2^{-\Delta\Delta CT}$ method. Primer sequences are provided in **Table S1**.

2.17. DC Activation

The activation of DCs was evaluated via flow cytometry, focusing on the expression of surface co-stimulatory molecules. BMDCs were seeded 5×10^5 cells per well in 12-well plates and incubated for 12 h before treatment with MnCl₂ solution, GAgel leachate, or GA@Mn leachate. Medium alone served as the negative control, and medium containing lipopolysaccharide (LPS, 10 μ g mL⁻¹) served as the positive control. After 24 h, cells were stained with anti-mouse CD11c-PerCP-Cy5.5, CD80-BV421, and CD86-PE-Cy7 antibodies. Samples were analyzed using a CytoFLEX LX flow cytometer (Beckman Coulter, USA), and the expression of CD80 and CD86 on CD11c⁺ cells was quantified.

2.18. Antigen Uptake

Antigen uptake was evaluated using confocal laser scanning microscopy (CLSM). BMDCs were seeded 5×10^5 cells per well onto glass coverslips and allowed to adhere. Medium alone served as the negative control. Cells were treated with MnCl₂, GAgel, and GA@Mn leachate containing 20 μ L OVA-FITC. After 12 h of incubation, cells were fixed with 4% paraformaldehyde for 15 min, stained with DAPI for 15 min at room temperature, and mounted for imaging. Fluorescence distribution of FITC-labeled antigen was visualized using CLSM (Zeiss LSM 980 with Airyscan 2, Germany), and antigen uptake was quantified based on fluorescence intensity.

2.19. Immune Cell Recruitment

Immune cell recruitment to the hydrogel injection site was assessed by histology and flow cytometry. Mice received subcutaneous injections

(200 μ L) of hydrogel. On day 5 post-injection, the nodule at injection site was excised, one portion was fixed in 4% paraformaldehyde, paraffin-embedded, sectioned, and stained with hematoxylin and eosin (H&E) for histological assessment. Paraffin sections were incubated with antibodies corresponding to CD11c, CD11b, Ly-6G, and CD49b for 12 h. After removing unbound antibodies, the sections were incubated with Cy3-conjugated goat anti-rabbit IgG and DAPI, respectively. Finally, the distribution of immune cells was observed and recorded using a confocal laser scanning microscope.

The remaining tissue was mechanically dissociated and digested for 3 h at 37 °C in 10 mL Hank's solution to prepare a single-cell suspension, which was counted and adjusted to 1×10^7 cells per millilitre. A 100 μ L aliquot was stained with antibodies against mouse CD11c-PerCP-Cy5.5, CD11b-PE-CF594, F4/80-PE, CD49b-APC, and Ly-6G-BV650. Stained cells were analyzed by flow cytometry to determine the proportions of DCs (CD11c⁺), macrophages (CD11b⁺F4/80⁺), NK cells (CD49b⁺), and neutrophils (Ly-6G⁺).

2.20. Specific Antibody and Neutralizing Antibody Assays

Foot-and-mouth disease virus-like particles (FMD VLPs) were employed as the antigen to prepare GAgel and GA@Mn hydrogel vaccines. Solution-based vaccines were formulated by dispersing FMD VLPs in PBS or MnCl₂ solution. PBS was used as control. Mice received a single immunization with an FMD VLP dose of 10 μ g per mouse. Serum antibody levels were measured using a liquid-phase blocking ELISA kits for FMD. 96 well plates were coated with 100 μ L per well of diluted FMDV-specific primary antibody and incubated overnight at 4 °C. Diluted serum samples pre-mixed with FMD VLPs were then added (100 μ L per well) and incubated at 37 °C for 30 min, followed by addition of IgG-HRP-conjugated secondary antibody (100 μ L per well) for 30 min. Color development was achieved with TMB substrate (100 μ L per well) for 15 min, and the reaction was stopped with 50 μ L per well of 2 M H₂SO₄. Absorbance at 450 nm was recorded using a Synergy H1 multimode microplate reader. Using

a liquid-phase blocking ELISA established with the single-domain antibody M8 and O-type FMD VLPs, the levels of neutralizing antibodies were assessed. In 96-well plates, 100 μ L of diluted antibody M8 was added to each well and incubated overnight at 4 °C. Subsequently, diluted serum samples pre-mixed with O-type VLPs antigen were added to the plates and incubated at room temperature for 1 h. Next, labeled M652 antibody was added and incubated at room temperature for 1 h. This was followed by the addition of HRP-conjugated secondary antibody and incubation at room temperature for 1 h. Finally, TMB substrate was added for color development, and the absorbance at 450 nm was measured using a microplate reader.

2.21. IgG1 and IgG2a Subtype

IgG1 and IgG2a levels in mouse serum were determined by indirect ELISA. Plates were coated overnight at 4 °C with 1 μ g per well of FMD VLPs, then blocked with 5% skim milk for 1 h. Diluted serum samples (100 μ L per well) were added and incubated at 37 °C for 1 h, followed by HRP-conjugated goat anti-mouse IgG1 or IgG2a antibodies for 1 h. TMB substrate (100 μ L per well) was added for 15 min, and the reaction was stopped with 50 μ L per well of 2 M H₂SO₄. Absorbance at 450 nm was measured using a Synergy H1 multimode microplate reader.

2.22. OVA-Specific Antibodies and Their Subtypes

To evaluate the antigen generality of the vaccine platform, immunization was performed using the model antigen ovalbumin (OVA). OVA antigen was loaded into GAgel and GA@Mn hydrogels to prepare OVA-GAgel and OVA-GA@Mn vaccines, respectively. Control vaccines were prepared by dispersing OVA in PBS or MnCl₂ solution. Mice received a single immunization with an OVA dose of 10 μ g per mouse. Serum was collected on day 28 post-immunization. Commercial mouse anti-OVA IgG, IgG1, and IgG2a ELISA kits were used to determine the levels of OVA-specific antibodies and antibody subtypes in the serum on day 28.

2.23. The mRNA Expression Levels of GC B

related Cytokines

View Article Online
DOI: 10.1039/D5NR04283F

Lymph nodes were harvested from mice and homogenized using Trizol reagent for RNA extraction. cDNA was synthesized following established protocols. The relative mRNA expression levels of GC B associated factors Bcl-6 and Bach2 were quantified via RT-PCR. GAPDH served as the reference gene, and the relative expression levels were calculated using the $2^{-\Delta\Delta CT}$ method. Primer sequences are provided in **Table S2**.

2.24. Isolation of Lymphocytes

Lymph node or spleen were aseptically removed, mechanically dissociated, and passed through a 200-mesh nylon screen. Single-cell suspensions were prepared using a murine lymphocyte density gradient separation kit (Dakewe, Beijing). After centrifugation at 800 g for 30 min, the lymphocyte layer was collected, washed with 10 mL RPMI 1640 medium, and centrifuged at 400×g for 5 min at 4 °C. The final cell suspension was adjusted to 1 \times 10⁷ cells per millilitre for further assays.

2.25. IL-4 and IFN- γ Secretion

The frequencies of IL-4- and IFN- γ -secreting splenic lymphocytes were determined using a mouse IL-4/IFN- γ precoated ELISpot kit. PVDF-membrane plates were equilibrated with 200 μ L per well of RPMI 1640 medium before seeding 1 \times 10⁶ per well cells of lymphocyte suspension. Cells were incubated for 18 h, followed by washing, conjugate addition, and substrate development according to the manufacturer's protocol. Spots representing cytokine-secreting cells were visualized and counted using an IRIS ASTOR ELISpot reader (Mabtech, Sweden).

2.26. GzmB Secretion

Granzyme B (GzmB) secretion by splenic lymphocytes from immunized mice was quantified using a mouse GzmB ELISA kit. Splenic lymphocyte suspensions were seeded at 1 \times 10⁵ per well cells in 96-well culture plates and stimulated with 2 μ g antigen for 18 h. After stimulation, supernatants were collected by centrifugation at 1000 g for 15 min at 4 °C. Aliquots were transferred to GzmB antibody-precoated plates, and



ARTICLE

Journal Name

subsequent assay steps were performed according to the manufacturer's instructions. Absorbance at 450 nm was measured using a microplate reader, and GzmB concentrations were calculated from the standard curve.

2.27. GC B, TCM, and TEM Cells

Lymphocytes were adjusted to 1×10^6 per well cells and analyzed by flow cytometry. The proportions of GC B cells ($B220^+CD95^+GL7^+$), central memory T cells (TCM, $CD44^+CD62L^+$), and central effector memory T cells (TEM, $CD44^+CD62L^-$) were determined.

2.28. *In Vivo* Biocompatibility

Hydrogel biocompatibility was assessed 56 days post-immunization by histopathological and hematological analyses. Mice were euthanized, and major organs (heart, liver, spleen, kidney, lung) were collected for H&E staining. Whole blood was analyzed for hematological parameters, including hemoglobin (HGB), mean corpuscular hemoglobin (MCH), mean corpuscular hemoglobin concentration (MCHC), mean corpuscular volume (MCV), red blood cell (RBC) count, and white blood cell (WBC) count. Serum was analyzed for biochemical indicators, including ALB, ALT, AST, CREA, UA, UREA.

3. Results and discussion

3.1. Mn^{2+} Coordinates with Natural Small Molecule GA to Form Hydrogel GA@Mn

Previous studies have demonstrated that the natural small molecule GA (Fig. 1a) can self-assemble into nanofibers and form a hydrogel GAgel (Fig. S1).²⁶⁻²⁸ In this work, we investigated the coordination-driven assembly between GA and Mn^{2+} (Fig. 1b). The vial inversion results showed that the addition of Mn^{2+} significantly promoted hydrogel formation. The stability of the GA@Mn hydrogel gradually increased with higher Mn^{2+} concentrations (Fig. 1c and Fig. S2). Considering the important influence of the hydrogel's mechanical properties on its function as an antigen depot, we selected the GA@Mn hydrogel formed with 5 mM Mn^{2+} for subsequent studies. SEM

images revealed that GA@Mn consists of abundant supramolecular nanofibers organized into a densely crosslinked network (Fig. 1d). Unbound Mn^{2+} was subsequently removed via three cycles of centrifugation (1500 g, 5 min), yielding purified GA@Mn nanofibers. EDS mapping confirmed the homogeneous distribution of Mn^{2+} throughout the nanofibers, alongside carbon (C), indicating stable coordination between Mn^{2+} and GA (Fig. 1e). ITC was further employed to quantify the Mn^{2+} -GA interaction. Titration of Mn^{2+} into GA solution produced an endothermic binding isotherm (Fig. 1f). Fitting the data to a one-site binding model (Fig. 1g) yielded N of 0.15, KD of 2.27×10^{-3} M, and ΔH of -2.17 kcal mol⁻¹, confirming and quantitatively characterizing the coordination interaction between GA and Mn^{2+} . Furthermore, FTIR analysis was conducted to investigate the interaction between GA and Mn^{2+} . The results (Fig. S3) showed that, compared to GAgel, the C=C stretching band in GA@Mn shifted to lower wavenumbers. Furthermore, the intensities of the O-H stretching band, -CH₃ stretching band, and C-O stretching band were reduced, indicating a strong binding interaction between GA and Mn^{2+} .²⁹⁻³⁰

Considering the widespread use of aluminum ions (Al^{3+}) in vaccine adjuvants, we also investigated the assembly between GA and Al^{3+} . Titration of Al^{3+} into the GA solution produced a distinct exothermic binding isotherm (Fig. S4). SEM images revealed that GA@Al also consists of a supramolecular nanofiber network (Fig. S5). EDS mapping similarly confirmed the homogeneous distribution of Al^{3+} alongside carbon (C) throughout the nanofibers, indicating a stable coordination between Al^{3+} and GA (Fig. S5). Finally, we examined the potential of Al^{3+} and GA to co-assemble into a hydrogel using different Al^{3+} concentrations. Vial inversion results (Fig. S6) indicated that a stable hydrogel forms when the Al^{3+} concentration reaches 1 mM. However, when the concentration increases to 5 mM, GA@Al exhibits some fluidity, suggesting that a higher dose of Al^{3+} is not conducive to forming a stable GA@Al hydrogel. These results demonstrate that Al^{3+} can coordinate with GA and form a stable hydrogel at appropriate concentrations. Unlike Al^{3+} , Mn^{2+} can activate the STING pathway and promote a Th1-biased immune response. Therefore,



in subsequent studies, we focused primarily on investigating the biological functions of GA@Mn.

3.2. Mn²⁺ Coordination Significantly Enhances the Mechanical Properties of the GA@Mn

The mechanical properties of hydrogel-based vaccine delivery systems are critical for both injectability and antigen depot formation.³¹ Here,

the strength of hydrogel was characterized via rheological measurements. The GAgel exhibited a broad LVR, with the G' and G'' intersecting at strains above 40%, after which G' dropped below G'', indicating a transition from hydrogel to sol state (Fig. 1h). In contrast, GA@Mn displayed a narrower LVR, transitioning at strains above 10%. Frequency and time sweep tests showed that the G' of GA@Mn was nearly three orders of magnitude higher than that of GAgel, with both G' and G''

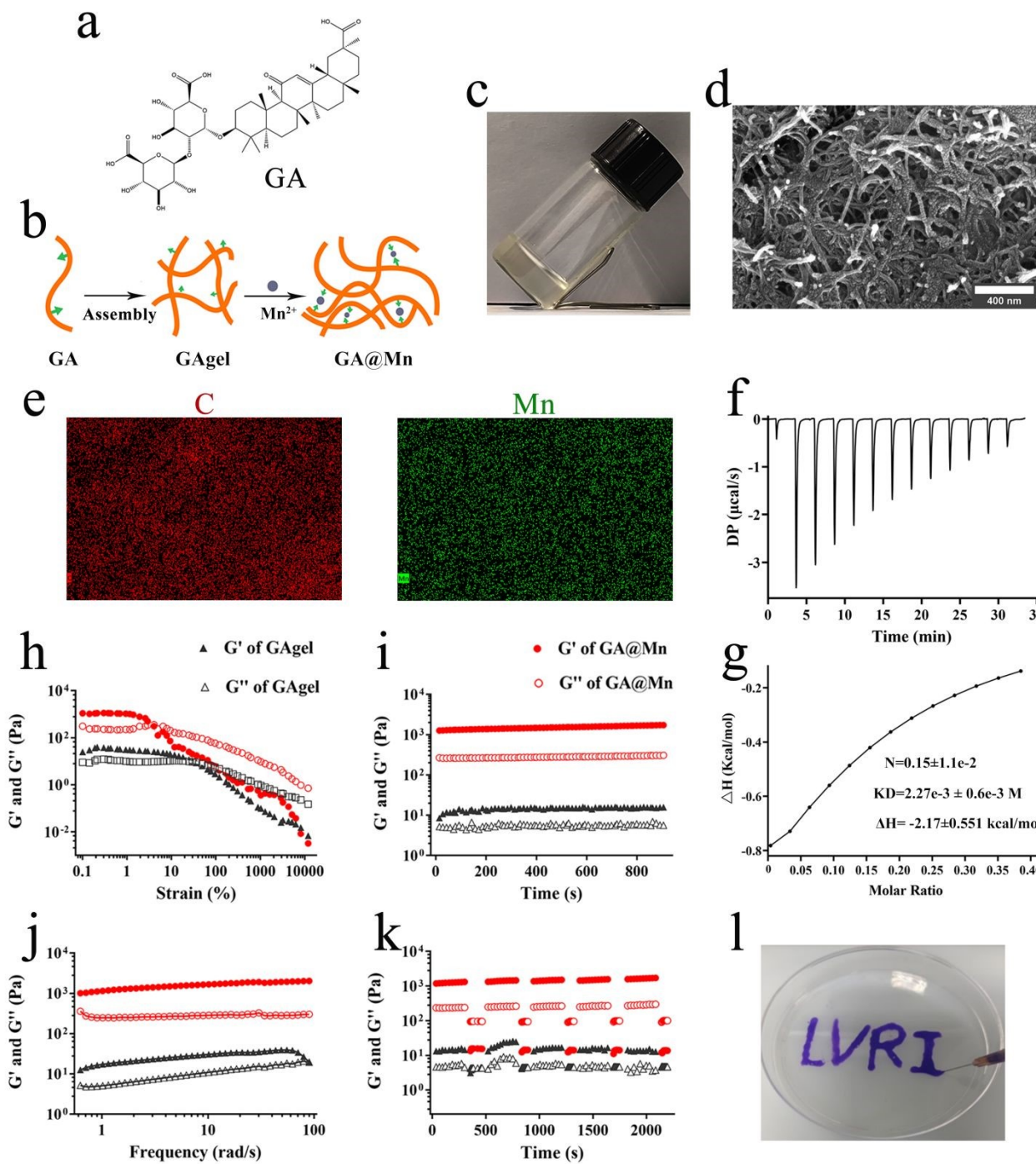


Fig. 1. Preparation and characterization of GA@Mn. **(a)** The chemical structure of GA. **(b)** Schematic illustration of GA@Mn preparation. **(c)** Optical image of GA@Mn. **(d)** SEM image of GA@Mn microstructure. **(e)** EDS elemental mapping of C or Mn in GA@Mn nanofibers. **(f-g)** Mn²⁺ titration curve with GA and thermodynamic parameters. **(h)** Strain sweep of GAgel and GA@Mn at 1 Hz. **(i)** Time sweep of GAgel and GA@Mn at 1% strain and 1 Hz. **(j)** Frequency sweep of GAgel and GA@Mn at 1% strain. **(k)** Step-strain test: alternating 1% strain (300 s) and 100% strain (60 s) for five cycles. **(l)** Photograph of "LVRI" extruded GA@Mn through syringe needle.



remaining stable throughout testing (**Fig. 1i and j**), demonstrating significantly enhanced mechanical strength, stability, and viscoelasticity. Creep-recovery tests under high strain (100%) followed by low strain (1%) showed that both hydrogels exhibited $G'' > G'$ under high strain, reflecting loss

of elastic behavior (**Fig. 1k**). Upon return to low strain, each hydrogel rapidly recovered its original mechanical properties, indicating efficient self-healing capability (**Fig. 1k**). This feature enables GA@Mn to promptly form a stable antigen depot at the injection site. Injectability was further

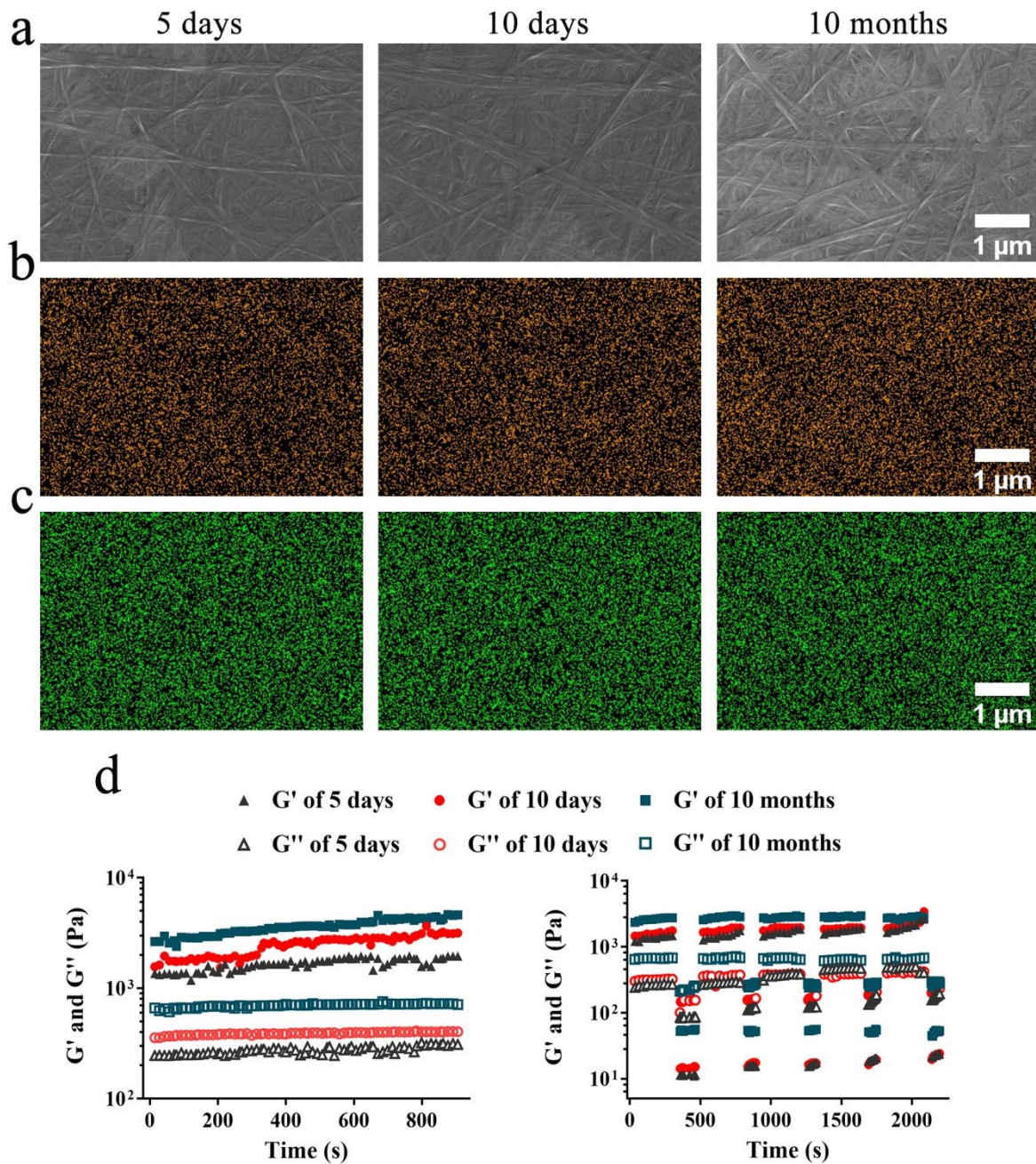


Fig. 2. Storage stability of the GA@Mn hydrogel. (a) SEM images of the microstructure of GA@Mn after storage at room temperature for 5 days, 10 days, and 10 months. (b-c) EDS elemental mapping showing the distribution of carbon (b) and manganese (c) in the nanofibers of GA@Mn after storage at room temperature for 5 days, 10 days, and 10 months. (d) Time sweep and step-strain tests performed on GA@Mn after storage at room temperature for 5 days, 10 days, and 10 months.

confirmed by extruding the GA@Mn through a 0.45 mm syringe needle, which produced continuous strands without rupture (**Fig. 11**), confirming its suitability for injection.

3.3. The GA@Mn Hydrogel Exhibits Excellent Storage Stability

The storage stability of a vaccine platform is crucial for its practical application. To further evaluate the application potential of GA@Mn, the hydrogel was stored at room temperature for 5 days, 10 days, and 10 months to assess its stability. Photographic results (**Fig. S7**) indicated that the GA@Mn hydrogel maintained good integrity even after 10 months of storage at room temperature. Furthermore, we observed the microstructure of GA@Mn after different storage periods using SEM. The SEM results (**Fig. 2a**) revealed that the GA@Mn hydrogel retained a network structure composed of stable supramolecular nanofibers even after 10 months of storage at room temperature. EDS mapping (**Fig. 2b-c**) showed a homogeneous distribution of Mn²⁺ and carbon (C) elements throughout the nanofibers, indicating that the stable coordination between Mn²⁺ and GA persisted. Time sweep tests (**Fig. 2d**) demonstrated that the G' values of GA@Mn remained significantly higher than the G" values and were stable throughout the testing period after storage for 5 days, 10 days, and 10 months. In step-strain tests (**Fig. 2d**), all tested samples exhibited the characteristic G">G' under high strain and rapidly recovered their original mechanical properties upon returning to low strain. This indicates that the GA@Mn hydrogel maintained excellent injectability after 5 days, 10 days, and even 10 months of storage at room temperature. Notably, under both testing modes, the G' values of the hydrogel stored for 10 months were higher than those stored for 5 or 10 days. This may be attributed to the formation of more stable cross-links within the nanofiber network over time.

3.4. Excellent Cytocompatibility of the GA@Mn

Biocompatibility is a fundamental requirement for hydrogel-based biomedical applications. To assess the cytocompatibility of GA@Mn, we incubated its leach solutions with BHK, DC2.4, and

Vero cells for 24 h. Cell viability was evaluated using the MTS assay, while live/dead staining was employed to examine morphological integrity. All treatment groups showed cell viability exceeding 95%, with no significant differences observed between groups (**Fig. S8a**), indicating that neither GAgel nor GA@Mn adversely affected cell proliferation. Live/dead staining images revealed intact cellular structures and normal morphology across all groups, comparable to the control (**Fig. S8b**). These results demonstrate the excellent cytocompatibility of GA@Mn and support its potential for further *in vivo* applications.

3.5. GA@Mn Enables Sustained Release of Antigen and Mn²⁺

Prolonged antigen release enhances immune responses by improving antigen bioavailability, extending interactions with immune cells, and promoting persistent GC activation.³² In this study, we first evaluated the *in vitro* degradation profiles of GAgel and GA@Mn, along with their respective

antigen and Mn²⁺ release behaviors (Fig. 3a). Hydrogels were incubated in PBS, with supernatants collected every 24 h to measure remaining mass, antigen concentration, and Mn²⁺ content. GAgel degraded completely within 12 days, while GA@Mn required 17 days (Fig. 3b).

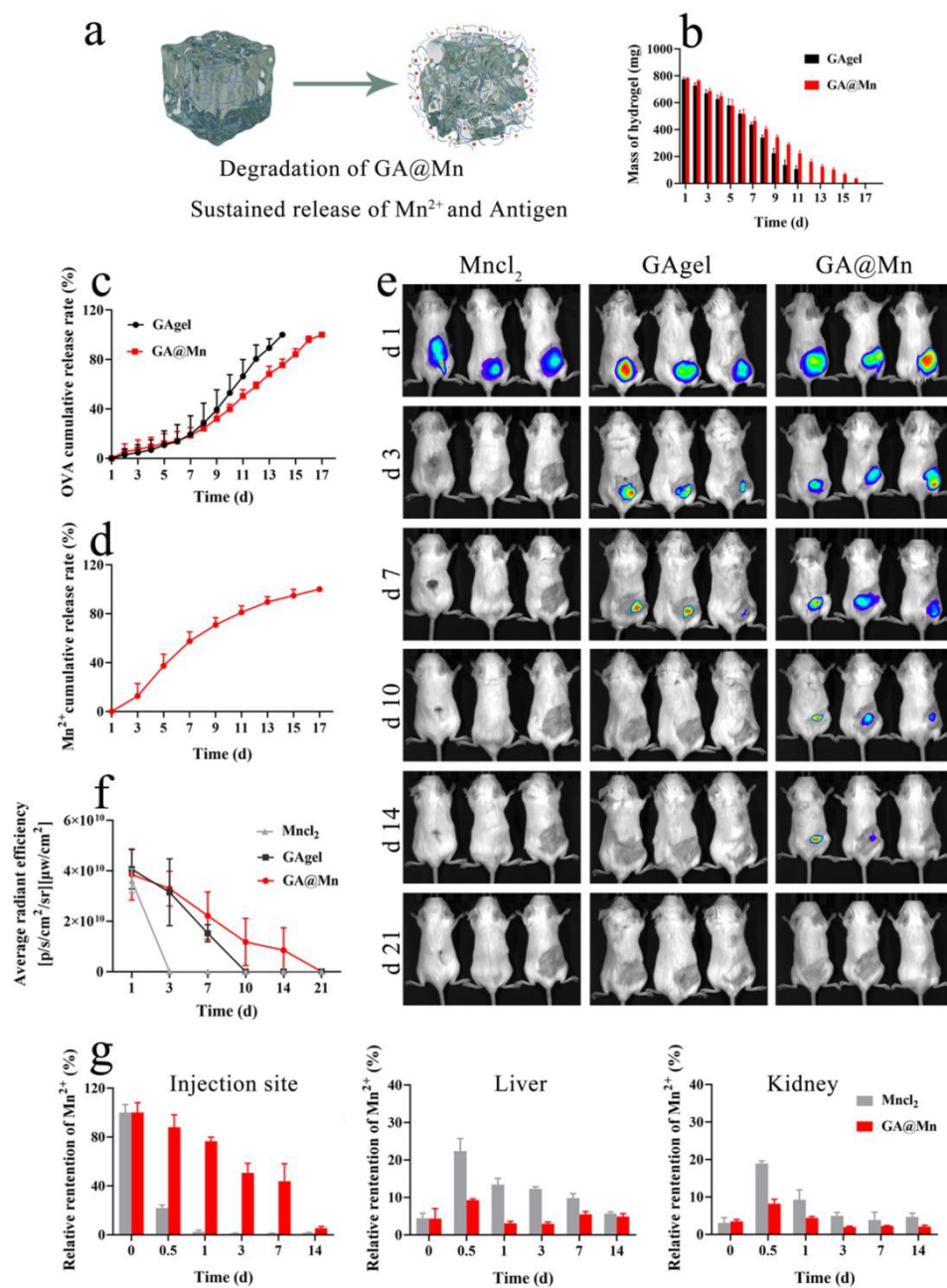


Fig. 3 GA@Mn sustained release of antigen and Mn²⁺ via gradual degradation *in vitro* and *in vivo*. (a) Schematic illustration of GA@Mn degradation and release profile of antigen and Mn²⁺. (b) *In vitro* degradation of GAgel and GA@Mn. (c) *In vitro* antigen release kinetics. (d) *In vitro* Mn²⁺ release kinetics from GA@Mn. (e) *In vivo* fluorescence images of mice injected with MnCl₂, GAgel, and GA@Mn containing FITC-OVA. (f) Quantification of fluorescence intensity at the injection site. (g) Mn²⁺ content at the injection site, Liver, and Kidney.

Antigen release correlated closely with matrix degradation: GAgel released its entire antigen payload by day 12 whereas GA@Mn completed release on day 17 (**Fig. 3c**). This synchronized release suggests that both hydrogels restrict rapid antigen leakage via their nanofiber networks, with GA@Mn's enhanced mechanical strength contributing to its more sustained profile. Similarly, Mn²⁺ release from GA@Mn was completed over 17 days (**Fig. 3d**). In contrast to free ions, which often leak rapidly, the coordination between Mn²⁺ and GA enables gradual release aligned with hydrogel disintegration. We next investigated antigen biodistribution *in vivo* using live imaging (**Fig. 3e**). Mice were subcutaneously administered Cy5-labeled OVA in MnCl₂ solution, GAgel, or GA@Mn. Fluorescence signals at the injection site were tracked using an *in vivo* imaging system (AniView 100). In the MnCl₂ group, fluorescence became nearly undetectable by day 3. The GAgel group showed fading signals from day 3 onward, with complete loss by day 10. In contrast, GA@Mn maintained detectable fluorescence for up to 14 days (**Fig. 3f** and **Fig. S9**), indicating significantly prolonged antigen retention attributable to enhanced depot formation. Sustained Mn²⁺ retention is equally critical for prolonged local immunostimulation and minimizing systemic exposure. We quantitatively assessed Mn²⁺ levels at the injection site and in major organs using ICP-MS. In the MnCl₂ group, Mn²⁺ was nearly undetectable locally after 3 days. In contrast, GA@Mn maintained significant Mn²⁺ levels at the site for 14 days (**Fig. 3g**), confirming that coordination with GA facilitates gradual Mn²⁺ release. Uncontrolled systemic diffusion of metal ions can lead to accumulation in various organs, particularly the liver and kidneys, which poses toxicity risks and hinders clinical translation.³²⁻³⁴ In this study, Mn²⁺ levels in major organs were quantified at days 0, 0.5, 1, 3, 7, and 14 post-injection. On day 0.5, the MnCl₂ group exhibited approximately two-fold higher hepatic and renal Mn²⁺ levels than the GA@Mn group; these levels returned to baseline by day 14. In GA@Mn-treated mice, organ-level Mn²⁺ remained consistently lower throughout the study (**Fig. 3g** and **Fig. S10a-c**), indicating controlled release that avoids systemic spikes and improves local bioavailability.

Furthermore, we collected serum from mice injected with MnCl₂ or GA@Mn at different time points post-injection to measure the Mn²⁺ concentration in the blood and changes in key biochemical indicators, aiming to assess potential bodily damage caused by the metabolism of the metal ion Mn²⁺. The change in serum Mn²⁺ levels (**Fig. S11**) showed that mice injected with the MnCl₂ solution experienced a rapid initial increase in blood Mn²⁺ concentration, followed by a gradual decrease. In contrast, the peak serum Mn²⁺ concentration in mice injected with GA@Mn was only one-third of that in the MnCl₂ group. Blood biochemical analysis results revealed that, compared to mice injected with GA@Mn, serum levels of AST, CREA, UA, and UREA were significantly higher in MnCl₂-injected mice at the measured time points (**Fig. S12**). This indicates that the rapid diffusion of metal ions in solution form can cause acute damage to the liver and kidneys in a short period. In summary, the enhanced mechanical properties of GA@Mn enable sustained codelivery of antigen and Mn²⁺ at the injection site. This synchronized release supports prolonged immunostimulation while reducing systemic exposure, offering a promising strategy for effective and safe vaccine adjuvant.³⁵

3.6. GA@Mn Activates the cGAS-STING Pathway, Promoting DC Maturation and Antigen Uptake

Mn²⁺ is known to activate the cGAS-STING pathway and promote immune cell maturation upon innate immune activation (**Fig. 4a**).³⁶ The application of cGAS-STING agonists, especially Mn²⁺, as vaccine adjuvants to bridge innate and adaptive immunity represents a promising research direction.³⁷ To evaluate whether GA@Mn activates APCs via the cGAS-STING pathway, DC2.4 cells were treated with GAgel leachates, GA@Mn leachates, or MnCl₂ solution. WB analysis showed that GA@Mn significantly increased the levels of p-STING and p-IRF3 compared to controls (**Fig. 4b** and **Fig. S13a-b**), confirming that GA@Mn preserves the bioactivity of Mn²⁺ and induces phosphorylation of key proteins in the STING pathway. Activated STING promotes the nuclear production of TANK-binding



kinase 1 (TBK1) (**Fig. 4b** and **Fig. S13c**), which can subsequently activate nuclear factor- κ B (NF- κ B) and stimulate type I interferon (IFN) secretion, thereby initiating innate immune responses. DC maturation serves as a critical link between innate and adaptive immunity. Mature DCs (mDCs)

upregulate co-stimulatory molecules such as CD80 and CD86, which are essential for antigen uptake and presentation.³⁸ BMDCs were incubated with GA@Mn or control materials, and maturation was assessed via flow cytometry. Consistent with earlier reports, Mn²⁺ alone markedly enhanced the

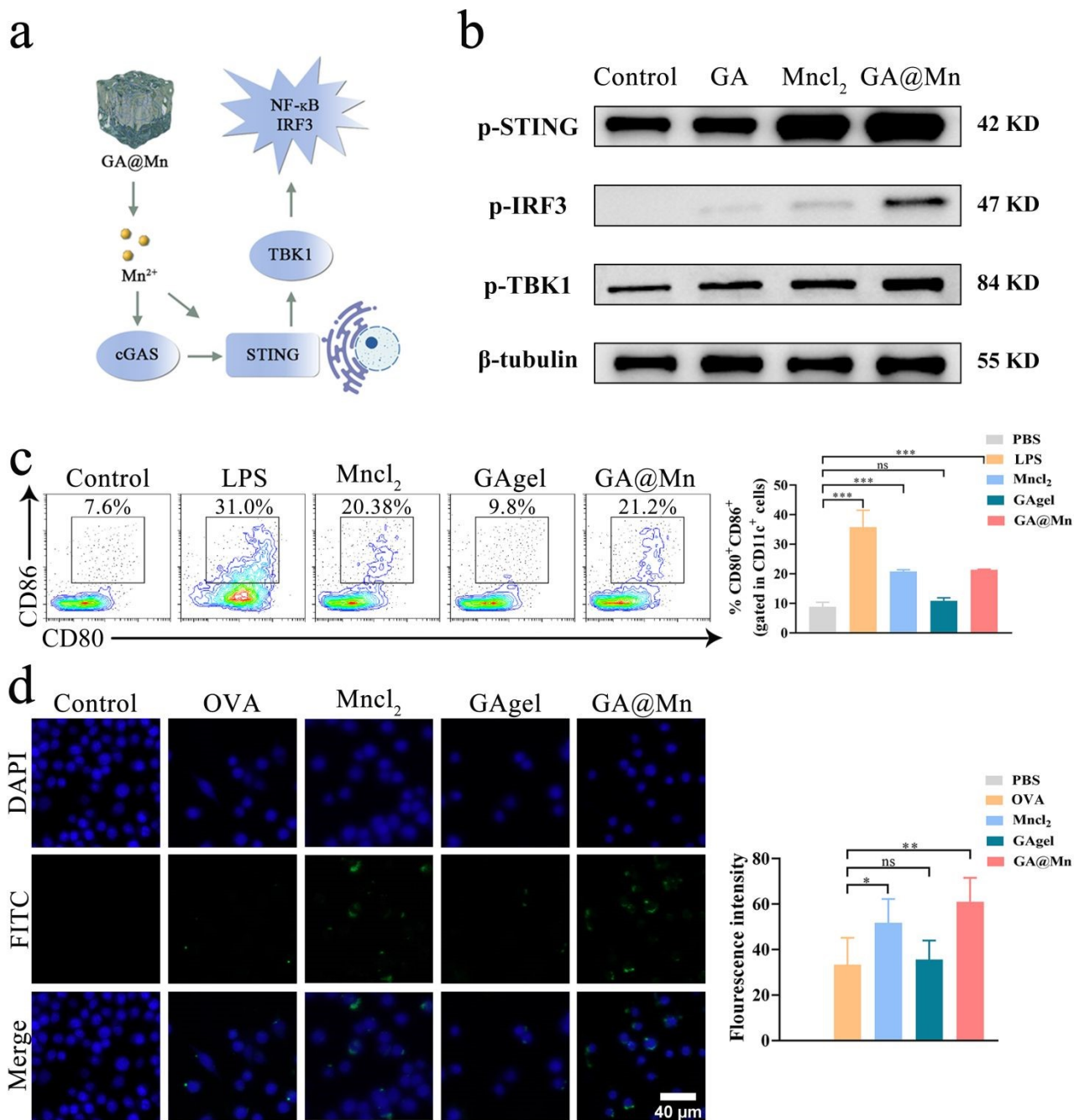


Fig. 4 GA@Mn activates the cGAS-STING pathway, promoting DC maturation and antigen uptake. **(a)** Schematic illustration of Mn²⁺-mediated cGAS-STING activation. **(b)** WB analysis of phosphorylation levels of cGAS-STING related signaling proteins in DC2.4. **(c)** Flow cytometry analysis of CD80⁺CD86⁺ DC11c cells. **(d)** CLSM analysis of FITC-OVA uptake by DCs. Scale bar: 40 μ m.

expression of CD80 and CD86, while GA@Mn induced the similar levels of both markers among all groups (**Fig. 4c**). Antigen uptake was evaluated by incubating BMDCs with FITC-OVA-loaded formulations. CLSM revealed stronger intracellular fluorescence in the MnCl₂ and GA@Mn groups (**Fig. 4d**), indicating enhanced antigen

internalization, which is a crucial step for subsequent antigen processing and presentation. We further evaluated the activation of cGAS-STING pathway activation by GA@Mn *in vivo*. Mice were subcutaneously injected 200 μ L of PBS, VLPs, MnCl₂, GAgel, or GA@Mn, respectively. Tissues from the injection site were collected 24 h

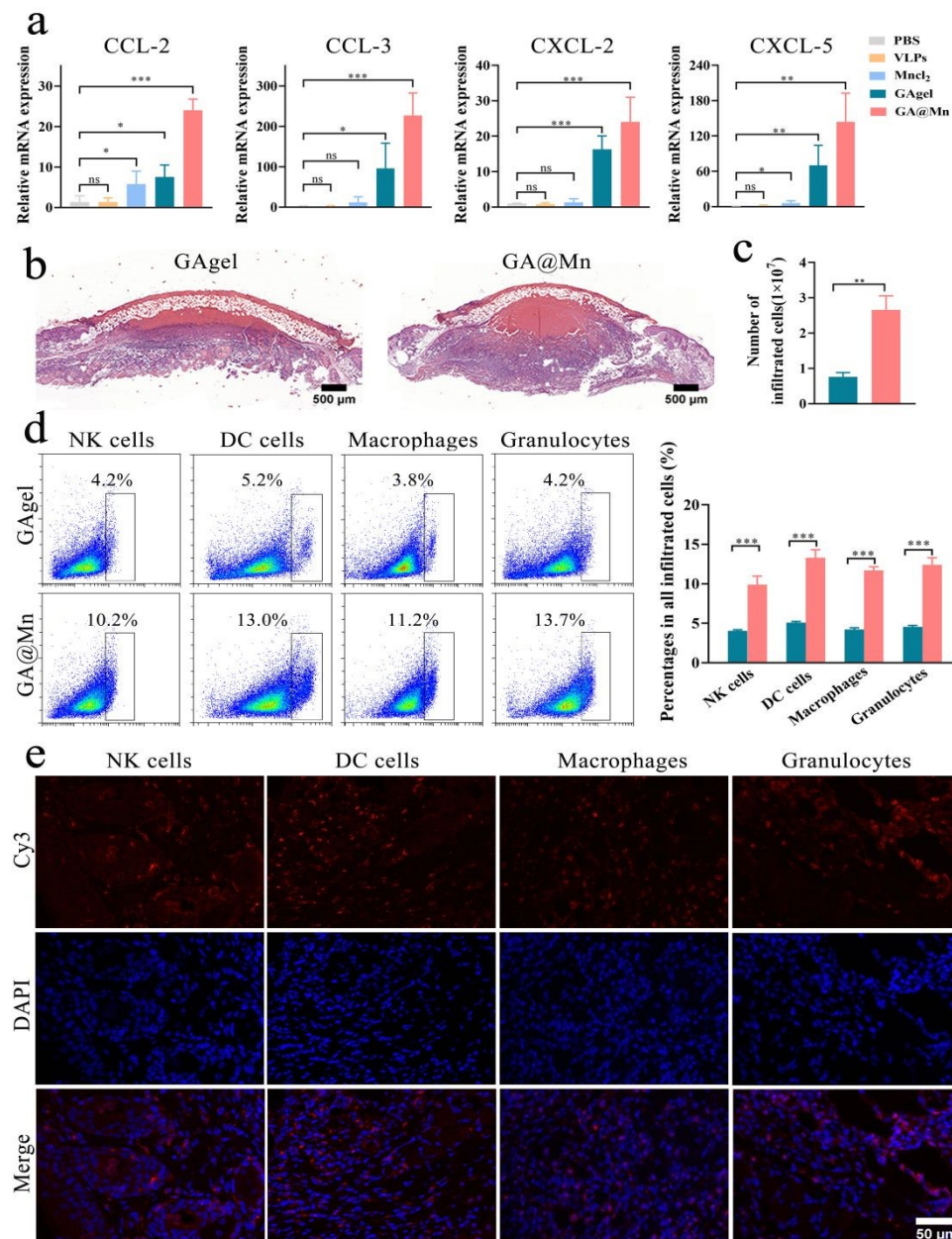


Fig. 5 GA@Mn promotes immune cell recruitment and facilitates a favorable immune microenvironment. **(a)** RT-PCR analysis of mRNA levels of CCL-2, CCL-3, CXCL-2, and CXCL-5 at the injection site of mice across treatment groups. **(b)** H&E staining of cell recruitment in GAgel and GA@Mn. **(c)** Quantification of total recruited cells in GAgel and GA@Mn. **(d)** Flow cytometry analysis of percentages of NK cells, DCs, macrophages and granulocytes among recruited cells in GAgel and GA@Mn. **(e)** Spatial distribution of NK cells, DC cells, macrophages and Granulocytes (red) in hydrogel GA@Mn. Nuclei were counterstained with DAPI (blue). Scale bar: 50 μ m.

ARTICLE

Journal Name

post-injection, and the expression of key cytokines related to the cGAS-STING pathway was analyzed using RT-qPCR. Both MnCl₂ and GA@Mn significantly upregulated the transcription of IRF3, NF-κB, and TBK1 (**Fig. S14**), confirming activation of the STING pathway. Moreover, GA@Mn induced higher expression of TNF-α and IL-6 compared to GAgel (**Fig. S15**), consistent with pro-inflammatory cytokine production driven by cGAS-STING activation.

3.7. GA@Mn Promotes APCs Recruitment and Establishes a Favorable Immune Microenvironment

In addition to detecting STING pathway activation, we examined chemokine expression at the injection site of mice via RT-qPCR. The GA@Mn hydrogel significantly upregulated the expression of CCL-2, CCL-3, CXCL-2, and CXCL-5 (**Fig. 5a**), suggesting its potential to promote immune cell recruitment.³⁹ To further evaluate immune cell recruitment, mice were subcutaneously injected with 200 μL of GAgel or GA@Mn. Five days post-injection, the hydrogels were excised for histological analysis and cellular quantification, while infiltrating immune subsets were characterized by flow cytometry. Macroscopically, GA@Mn elicited pronounced cellular infiltration with the formation of distinct nodules (**Fig. S16**). H&E staining revealed that immune cells in GAgel were largely restricted to the periphery of the scaffold, whereas GA@Mn supported extensive and uniform infiltration throughout the hydrogel matrix (**Fig. 5b**), demonstrating its superior capacity for immune cell recruitment and penetration. Quantitative analysis confirmed a significantly higher number of recruited cells in GA@Mn compared to GAgel (**Fig. 5c**). Flow cytometry further indicated that immune cells accounted for up to 40% of the total cells recruited by GA@Mn, including DCs (13.0%), macrophages (11.2%), granulocytes (13.7%), and NK cells (10.2%) (**Fig. 5d**). Notably, APCs constituted the predominant population among the recruited cells, forming an immune-favorable niche conducive to the initiation and amplification of adaptive immunity. To spatially

resolve the immune microenvironment constructed by the GA@Mn hydrogel, ^{DOI: 10.1039/DENB04283F} we performed immunofluorescence staining on sections from the injection site. Consistent with the widespread cellular infiltration indicated by H&E staining, fluorescence imaging visually revealed the distribution characteristics of recruited immune cells within the GA@Mn hydrogel matrix. The immunofluorescence imaging results showed that NK cells, DCs, macrophages, and granulocytes exhibited a uniform, diffuse distribution throughout the internal scaffold of the hydrogel (**Fig. 5e**). This spatial distribution pattern further indicates that the GA@Mn hydrogel can effectively recruit various immune cells to the injection site, creating an immune microenvironment conducive to antigen processing and presentation.

3.8. GA@Mn Promotes GC Formation and Induces Potent Humoral Immunity



Having established that GA@Mn activates innate immunity and recruits immune cells *in vivo* to establish an immunologically favorable microenvironment, we next evaluated its capacity to induce antigen-specific adaptive immune responses in mice. FMD VLPs were employed as the antigen to prepare GAgel and GA@Mn hydrogel vaccines. Solution-based vaccines were formulated by dispersing FMD VLPs in PBS or MnCl₂ solution. Mice received a single immunization dose (Fig. 6a), and both humoral and cellular immune responses were assessed. GC

reactions play a pivotal role in humoral immunity by facilitating the positive selection and clonal expansion of B cells, leading to high-affinity antibody production.⁴⁰ The expression of transcription factors Bcl6 and Bach2 is closely linked to GC formation and serves as a key indicator of GC activation. On day 7 post-immunization, RNA extracted from lymph node cells of immunized mice was analyzed via RT-qPCR. GA@Mn significantly upregulated Bcl6 and Bach2 expression compared to FMD VLPs alone (Fig. S17), indicating robust GC activation. Flow

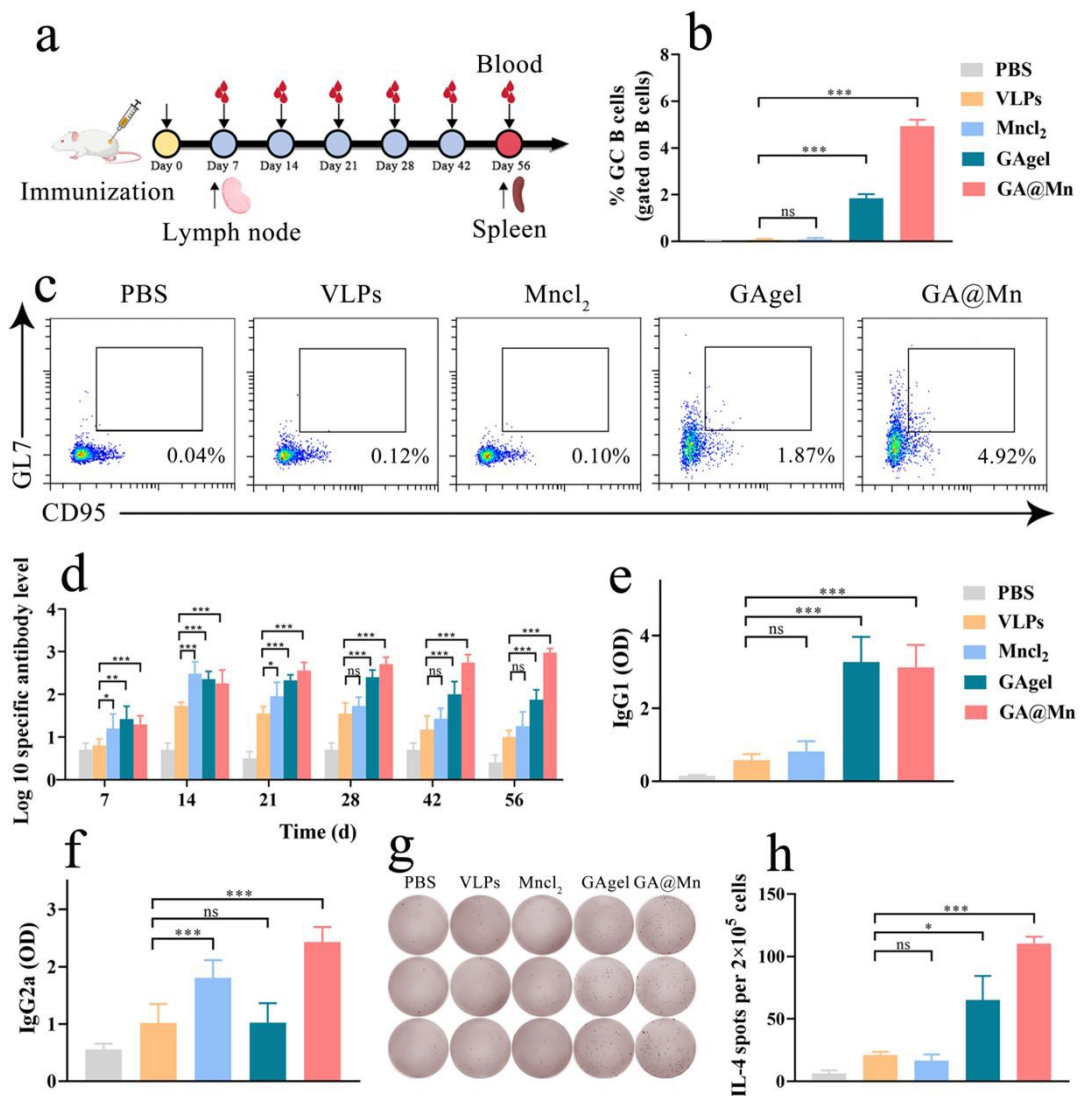


Fig. 6 GA@Mn promotes GC formation and elicits potent humoral immunity. (a) Schematic of immunization and serum collection schedule. (b-c) Flow cytometry analysis of GC B cells in lymph nodes at one week post-injection. (d) ELISA of antigen-specific IgG titers in serum. (e-f) Indirect ELISA of IgG1 and IgG2a levels in serum. (g-h) ELISpot analysis of IL-4-secreting splenocytes after antigen restimulation.

cytometric analysis of lymph nodes further revealed that the GA@Mn group had a markedly higher proportion of GC B cells, which was 2.6-fold greater than that in the GAgel group (**Fig. 6b and c**), likely attributable to its enhanced antigen depot effect.

Serum samples collected at designated time points were evaluated for antigen-specific IgG titers. At day 14, the MnCl₂-formulated VLPs solution vaccine induced the highest IgG titers, though these levels declined rapidly thereafter. GAgel elicited lower and transient antibody responses, likely due to the absence of Mn²⁺ adjuvant and its limited mechanical stability. In contrast, GA@Mn produced gradually increasing, high-level, and sustained antigen-specific antibody titers (**Fig. 6d**), demonstrating that its hydrogel scaffold enhances both the magnitude and

durability of humoral immunity through sustained release of antigen and Mn²⁺. DOI: 10.1039/D5NR04283F

To further characterize the humoral response, we profiled IgG subclasses, which reflect distinct immune polarizations. VLPs alone primarily induced a Th2-biased IgG1 response, while the addition of Mn²⁺ increased IgG2a levels. GAgel similarly elicited an IgG1-dominated profile (**Fig. 6e and f**). Notably, GA@Mn generated the highest levels of both IgG1 and IgG2a, suggesting a mixed Th1/Th2 humoral immune phenotype. On day 56, ELISpot analysis revealed that GAgel increased the number of antigen-specific IL-4-secreting cells by 3.1-fold compared to VLPs alone, whereas GA@Mn induced a 5.2-fold increase (**Fig. 6g and h**), further corroborating that Mn²⁺ coordination enhances the hydrogel's antigen depot functionality and amplifies humoral immunity.

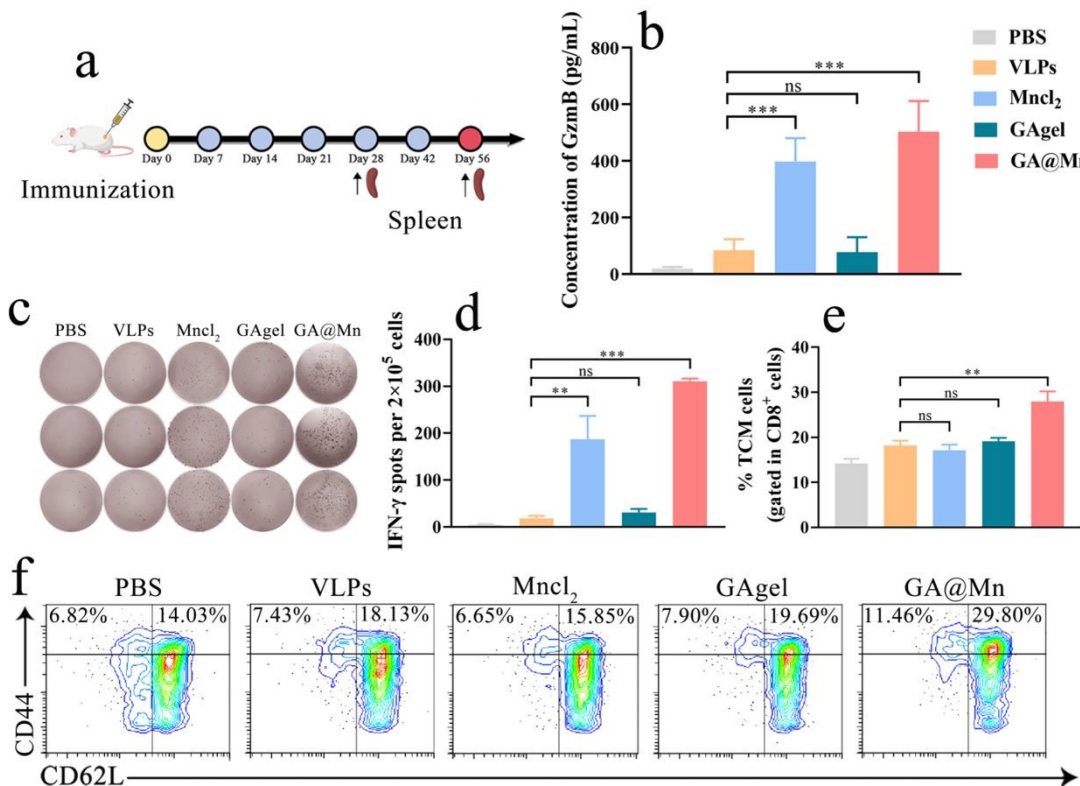


Fig. 7 GA@Mn promotes cellular immunity. **(a)** Schematic of immunization and sample collection schedule. **(b)** ELISA of GzmB levels across treatment groups. **(c-d)** ELISpot analysis of IFN- γ -secreting splenocytes after antigen restimulation. **(e-f)** Flow cytometry of TCM percentages among splenic CD8⁺ T cells.

To further evaluate the ability of GA@Mn to enhance vaccine immunogenicity, we analyzed the neutralizing antibody levels in serum on day 28 post-immunization. Compared to the MnCl₂ solution and the GAgel hydrogel, GA@Mn maximally increased the neutralizing antibody levels, achieving a neutralizing antibody titer of 2.3 Log₁₀ (**Fig. S18**). Based on the correlation we previously established,⁴¹ it can be estimated that GA@Mn formulated with FMD VLPs can provide approximately 84% protection against challenge at 28 days post-immunization. To assess the broad applicability of GA@Mn, we further immunized mice with the model antigen OVA. On day 28 post-immunization, the GAgel hydrogel and MnCl₂ solution moderately increased the levels of OVA-specific antibodies and their IgG1 and IgG2a subtypes to varying degrees (**Fig. S19**). GA@Mn demonstrated the highest capability in enhancing specific antibody and subtype levels, indicating that the GA@Mn vaccine delivery system is also applicable to the model antigen OVA.

3.9. GA@Mn Amplifies Cellular Immunity and Immunological Memory

Mn²⁺ activates the STING pathway, stimulates IFN- γ production, and plays a pivotal role in cellular immune activation.⁴² To evaluate the cellular immune response induced by GA@Mn, splenic lymphocytes were isolated from immunized mice on day 28 post-immunization, and antigen-specific cytotoxic T lymphocyte (CTL) activity was assessed via GzmB level (**Fig. 7a**). The GA@Mn group exhibited the highest GzmB concentration, exceeding that of the VLP, MnCl₂, and GAgel groups by 6.6-fold, 1.2-fold, and 6.5-fold, respectively (**Fig. 7b**), indicating a substantially enhanced antigen-specific T cell response. The frequency of antigen-specific IFN- γ -producing cells was further evaluated using ELISpot. Consistent with the CTL results, GA@Mn immunization induced a markedly higher number of IFN- γ -secreting cells compared to all other groups (**Fig. 7c and d**), confirming that Mn²⁺ coordination enhances the hydrogel's ability to promote cellular immunity. Immune memory is critical for rapid and potent responses upon

pathogen re-exposure. TEM and TCM contribute to long-term immunity by mediating swift and robust recall responses.⁴³ On day 56 post-immunization, splenic memory T cell subsets were analyzed by flow cytometry. GA@Mn immunization significantly increased the proportions of both TEM and TCM compared to all other treatments (**Fig. 7e, f and Fig. S20**), demonstrating its capacity to establish durable immune memory. These results indicate that GA@Mn not only enhances effector T cell responses but also facilitates the generation of long-lived memory T cell subsets. This effect is likely due to the sustained release of antigen and Mn²⁺ from the hydrogel, which provides prolonged immunostimulation and supports the development of lasting immune memory.

3.10. Excellent *in vivo* Biocompatibility of GA@Mn

The *in vivo* biocompatibility of GA@Mn is critical for its further development and potential clinical translation. To evaluate its safety profile, blood samples and major organs (heart, liver, spleen, kidney, and lung) were collected from mice 56 days after immunization. Comprehensive assessments were conducted through hematological analysis, serum biochemistry, and histopathological examination. All hematological parameters, including HGB, MCH, MCHC, MCV, RBC, and WBC, remained within normal physiological ranges across all experimental groups (**Fig. S21a**). Similarly, serum biochemical markers such as ALB, ALT, AST, CREA, UA, and UREA also fell within normal reference values in all treatments (**Fig. S21a**). Histological evaluation further confirmed the absence of pathological changes or structural abnormalities in the major organs of GA@Mn-treated mice compared to controls (**Fig. S21b**). Together, these results demonstrate that GA@Mn does not induce detectable toxicity or adverse effects in major organ systems, hematopoiesis, or liver function, underscoring its excellent biocompatibility and strong potential for clinical application.

4. Conclusions



ARTICLE

Journal Name

In this study, we engineered a GA@Mn hydrogel-based vaccine delivery platform through coordination-driven self-assembly of GA and Mn²⁺. The incorporation of Mn²⁺ not only facilitated GA supramolecular organization but also significantly enhanced the mechanical robustness of the resulting hydrogel, effectively addressing the limited structural stability typical of small-molecular hydrogels and substantially prolonging antigen persistence at the injection site. Crucially, Mn²⁺ was stably integrated into the nanofiber network not merely by physical encapsulation but via coordination binding. This approach enabled a sustained release of Mn²⁺ that was synchronized with hydrogel degradation, ensuring prolonged immunostimulation. Meanwhile, this platform facilitated substantial recruitment of immune cells and the establishment of a favorable microenvironment conducive to antigen presentation. Moreover, GA@Mn activated the cGAS-STING pathway, enhanced DC maturation and antigen uptake, and ultimately provoked robust antigen-specific humoral and cellular immune responses following a single administration.

By synergizing the Th1-biased immunity driven by Mn²⁺ with the depot-based Th2-polarization capability of the hydrogel, GA@Mn represents a well-defined, mechanistically elucidated, and highly potent vaccine delivery system with significant promise for clinical translation.

Author contributions

Jingjing Zhou: Investigation, Methodology, Formal analysis, Validation, Writing-original draft, Funding acquisition. **Shengying Zhang:** Methodology, Formal analysis, Validation. **Hu Dong:** Methodology, Formal analysis. **Yunhua Li:** Methodology. **Haoyue Zang:** Methodology, Validation. **Zhidong Teng:** Methodology. **Mingyang Zhang:** Methodology. **Yifan Liu:** Methodology. **Shiqi Sun:** Investigation, Funding acquisition, Writing-review & editing. **Huichen Guo:** Conceptualization, Funding acquisition, Writing-review & editing.

Conflicts of interest

View Article Online
DOI: 10.1039/D5NR04283F

There are no conflicts to declare.

Data availability

The data are available upon reasonable request.

Acknowledgements

This work was supported by grants from the National Natural Science Foundation of China (Nos. 32301127 and 32473012). The Natural Science Foundation of Gansu Province (Nos. 25JRRA442 and 25JRRA1089) and Gansu Longyuan Youth Innovation and Entrepreneurship Talent Program-Youth Team (No. 2025QNTD34).

Notes and references

- 1 Y. Sheng, Z. Li, X. Lin, L. Wang, H. Zhu, Z. Su and S. Zhang, *J. Control. Release.*, 2024, 368, 275-289.
- 2 X. Fan, F. Liu, F. Sun, Y. Wang, W. Shen, S. Wang, J. Sun and K. Wang, *Acta Pharm. Sin. B.*, 2025, 9, 4644-4672.
- 3 R. Guyon, S. Reinke, A. Truby, L. Sims, A.V.S. Hill, L. Bau, E. Stride and A. Milicic, *Sci. Transl. Med.*, 2025, 17, eadw2256.
- 4 H. Jia, J. Lin, D. Wang, X. Lv, Q. Wang, Z. Wang, J. Liu, L. Yang and J. Liu, *Adv. Funct. Mater.*, 2024, 34, 2315442.
- 5 P. Wang, Y. Wang, H. Li, M. Wang, Y. Wang, X. Wang, L. Ran, H. Xin, J. Ma, G. Tian, W. Gao and G. Zhang, *Acta Biomater.*, 2024, 177, 400-413.
- 6 R. Zhang, C. Wang, Y. Guan, X. Wei, M. Sha, M. Yi, M. Jing, M. Lv, W. Guo, J. Xu, Y. Wan, X.M. Jia and Z. Jiang, *Cell. Mol. Immunol.*, 2021, 18, 1222-1234.
- 7 K.M. Garland, T.L. Sheehy and J.T. Wilson, *Chem. Rev.*, 2022, 122, 5977-6039.
- 8 L. Yang, Y. Wang, Y. Song, Z. Li, L. Lei, H. Li, B. He, J. Cao and H. Gao, *J. Control. Release.*, 2024, 370, 354-366.
- 9 Y. Zhao, X. Zhao, X. Wang, Z. Ma, J. Yan, S. Li, N. Wang, J. Jiao, J. Cui and G. Zhang, *Acta Biomater.*, 2025, 193, 417-428.
- 10 M.E. Aikins, X. Sun, H. Dobson, X. Zhou, Y. Xu, Y.L. Lei, and J.J. Moon, *J. Control. Release.*, 2024, 368, 768-779.
- 11 H. Hao, S. Wu, J. Lin, Z. Zheng, Y. Zhou, Y. Zhang, Q. Guo, F. Tian, M. Zhao, Y. Chen, X. Xu, L. Hou, X. Wang and R. Tang, *Nat. Biomed. Eng.*, 2023, 7, 928-942.
- 12 X. Dong, P. Pan, Q. Zhang, J.J. Ye and X.Z. Zhang, Engineered living bacteriophage-enabled self-adjuvanting hydrogel for remodeling tumor microenvironment and cancer therapy, *Nano Lett.*, 2023, 23, 1219-1228.
- 13 V.H. Giang Phan, H.T.T. Duong, T. Thambi, T.L. Nguyen, M.H. Turabee, Y. Yin, S.H. Kim, J. Kim, J.H. Jeong and D.S. Lee, *Biomaterials*, 2019, 195, 100-110.
- 14 X.X. Li, Y.Z. Wang, S.W. Wang, C.H. Liang, G.J. Pu, Y.X. Chen, L. Wang, H. Xu, Y. Shi and Z. Zhang, *Nanoscale*, 2020, 12, 2111-2117.



Journal Name

15 Z.Y. Wang, C.H. Liang, F. Shi, T. He, C.Y. Gong, L. Wang, and Z. Zhang, *Nanoscale*, 2017, 9, 14058- 14064.

16 C. Korupalli, W.Y. Pan, C.Y. Yeh, P.M. Chen, F.L. Mi, H.W. Tsai, Y. Chang, H.J. Wei and H.W. Sung, *Biomaterials*, 2019, 216, 119268.

17 C. Zhang, E. Cai, X. Qi, X. Ge, Y. Xiang, J. Wang, Y. Li, L. Lv, H. Zheng, Y. Qian, W. Dong, H. Li and J. Shen, *Chem. Eng. J.*, 2024, 487, 150756.

18 W. Luo, Z. Yang, J. Zheng, Z. Cai, X. Li, J. Liu, X. Guo, M. Luo, X. Fan, M. Cheng, T. Tang, J. Liu and Y. Wang, Small molecule hydrogels loading small molecule drugs from chinese medicine for the enhanced treatment of traumatic brain injury, *ACS Nano*, 2024, 18, 28894-28909.

19 K. Chen, X. Wu, Q. Wang, Y. Wang, H. Zhang, S. Zhao, C. Li, Z. Hu, Z. Yang and L. Li, *Chem. Lett.*, 2023, 34, 107446.

20 Y. Qian, Y. Zheng, J. Jin, X. Wu, K. Xu, M. Dai, Q. Niu, H. Zheng, X. He, J. Shen, *Adv. Mater.*, 2022, 34, e2200521.

21 W. Liu, Z. Li, Z. Wang, Z. Huang, C. Sun, S. Liu, Y. Jiang and H. Yang, *ACS Appl. Mater. Interfaces*, 2023, 15, 7767-7776.

22 X. Yu, J. Cai, M. Xu, Q. Li, Y. Yang, Z. Wan and X. Yang, *Nanoscale*, 2024, 16, 14261-14268.

23 W. Xu, Z. Lin, C.J. Kim, Z. Wang, T. Wang, C. Cortez-Jugo and F. Caruso, *Sci. Adv.*, 2024, 10, eads9542.

24 T. Guan, Z. Chen, X. Wang, S. Gao, X. Lu, Y. Li, Z. Wang, S. Zhang, Y. Guo, M. Guo, Y. Cui, Y. Wang and C. Chen, *J. Am. Chem. Soc.*, 2025, 147, 6523-6535.

25 H. Guo, S. Sun, Y. Jin, S. Yang, Y. Wei, D. Sun, S. Yin, J. Ma, Z. Liu, J. Guo, J. Luo, H. Yin, X. Liu and D. Liu, *Vet. Res.*, 2013, 44, 1-13.

26 X. Zhao, H. Zhang, Y. Gao, Y. Lin and J. Hu, *ACS Appl. Bio Mater.*, 2020, 3, 648-653.

27 J. Hao, Y. Gao, J. Liu, J. Hu and Y. Ju, *ACS Appl. Mater. Interfaces*, 2020, 12, 4927-4933.

28 X. Yu, M. Xu, J. Cai, Q. Li, Y. Yang, Z. Wan and X. Yang, *Giant*, 2024, 17, 100240.

29 E. Su, Q. Li, M. Xu, Y. Yuan, Z. Wan, X. Yang and B.P. Binks, *J. Colloid Interface Sci.*, 2020, 11.

30 Y. Qian, Y. Zheng, J. Jin, X. Wu, K. Xu, M. Dai, Q. Niu, H. Zheng, X. He and J. Shen, *Adv. Mater.*, 2022, 2200521, 1-15.

31 H. Song, Q. Su, Y. Nie, C. Zhang, P. Huang, S. Shi, Q. Liu and W. Wang, *Acta Biomater.*, 2023, 158, 535-546.

32 X. Sun, X. Zhou, X. Shi, O.A. Abed, X. An, Y.L. Lei and J.J. Moon, *Nat. Biomed. Eng.*, 2024, 8, 1073-1091.

33 X. Liu, Y. Liu, X. Yang, X. Lu, X.N. Xu, J. Zhang and R. Chen, *ACS Appl. Mater. Interfaces*, 2023, 15, 48871-48881.

34 J.H. Lee, H.J. Sutton, C.A. Cottrell, I. Phung, G. Ozorowski, L.M. Sewall, R. Nedellec, C. Nakao, M. Silva, S.T. Richey, J.L. Torres, W.H. Lee, E. Georgeson, M. Kubitz, S. Hodges, T.M. Mullen, Y. Adachi, K.M. Cirelli, A. Kaur, C. Allers, M. Fahlberg, B.F. Grasperge, J.P. Dufour, F. Schiro, P.P. Aye, O. Kalyuzhniy, A. Liguori, D.G. Carnathan, G. Silvestri, X. Shen, D.C. Montefiori, R.S. Veazey, A.B. Ward, L. Hangartner, D.R. Burton, D.J. Irvine, W.R. Schief and S. Crotty, *Nature*, 2022, 609, 998-1004.

35 B.S. Ou, O.M. Saouaf, J. Yan, T.U.J. Bruun, J. Baillet, X. Zhou, N.P. King and E.A. Appel, *Adv. Healthc. Mater.*, 2023, 12, e2301495.

36 X. Zhang, X.C. Bai and Z.J. Chen, *Immunity*, 2020, 12, 33, 43-53.

37 Q.R. Li, X. Zhang, C. Zhang, Y. Zhang, M.T. Niu, Z. Chen, S.M. Zhang, J. He, W.H. Chen and X.Z. Zhang, *J. Am. Chem. Soc.*, 2025, 147, 24555-24572.

38 S.H. Zhou, R.Y. Zhang, Z.W. You, Y.K. Zou, Y. Wen, J. Wang, D. Ding, M.M. Bian, Z.M. Zhang, H. Yuan, G.F. Yang and J. Guo, *ACS Appl. Mater. Interfaces*, 2023, 15, 8914-8926.

39 W. Fu, M. Guo, X. Zhou, Z. Wang, J. Sun, Y. An, T. Guan, M. Hu, J. Li, Z. Chen, J. Ye, X. Gao, G.F. Gao, L. Dai, Y. Wang and C. Chen, *ACS Nano*, 2024, 18, 11200-11216.

40 J. Deng, Z. Wang, L. Wu, Z. Song, H.S. Baholol, X. Li, L. Zhao and H. Han, *ACS Nano*, 2025, 19, 9042-9052.

41 H. Li, A. Dekker, Y. Zhang, Y. Zhang, M. Harmsen, W. Poel, H. Guo, and S. Sun, *Vaccine*, 2025, 62, 1-5.

42 C. Dong, Y. Wang, W. Zhu, Y. Ma, J. Kim, L. Wei, G.X. Gonzalez and B.Z. Wang, *ACS Appl. Mater. Interfaces*, 2022, 14, 6331-6342.

43 X. Deng, T. Liu, Y. Zhu, J. Chen, Z. Song, Z. Shi and H. Chen, *Bioact. Mater.*, 2024, 33, 483-496.

View Article Online



Data availability

All data supporting this findings of this study are available within the article and its Supplementary Information (SI).